A comparison of photodeposited RuO_x for alkaline water electrolysis

Katelkynn M. Daly,[†,‡] Santiago Jimenez-Villegas,[†,‡] Ben Godwin,[†,¶] Martin A. W. Schoen,[†] Oliver Calderon,[†] Ning Chen,[§] and Simon Trudel[*,†]

†*Department of Chemistry and Institute for Quantum Science and Technology, University of Calgary, 2500 University Dr NW, Calgary, AB, Canada*

‡*both authors contributed equally*

¶*Now at: Department of Chemistry, University of Victoria, Victoria, BC, Canada*

§*Hard X-ray Micro-Analysis Beamline, Canadian Light Source, 44 Innovation Boulevard, Saskatoon, SK S7N 2V3, Canada*

E-mail: trudels@ucalgary.ca

Phone: +1.403.210.7078

Abstract

The storage of renewable energy is a pressing challenge to overcome in the transition towards a power grid based on plentiful, yet intermittent energy supplies. The renewables-driven electrolysis of water to form hydrogen fuel is an attractive avenue, but requires better oxygen-evolution reaction (OER) catalysts to be feasible at scale. RuO_2 is touted as one of the superior OER catalysts, but only under acidic conditions – RuO_2 electrocatalysts suffer from poor stability under alkaline conditions. In this work, we evaluate three photodeposited RuO_2 OER electrocatalysts, all prepared via a scalable photodeposition method. Based on electrochemical and spectroscopic studies (x-ray photoelectron spectroscopy and X-ray absorption spectroscopy) our main findings are that nanocrystalline RuO_2 catalysts

outperform their amorphous counterpart, and are stable under alkaline (0.1 M KOH) conditions. This works thus lifts a major hurdle towards the use of RuO_2 for alkaline water electrolysis.

Keywords: ruthenium oxide, amorphous materials, oxygen evolution reaction, low-temperature thin film deposition

1 Introduction

We need to aggressively curb climate change.[1] The energy sector – which accounts for approximately 35% of total anthropogenic greenhouse gas emissions[2] – heavily relies on fossil fuels.[3] Meanwhile, global energy consumption is projected to at least double by 2050,[4,5] illustrating the pressing need for sustainable and greenhouse gas emission-free energy cycles. Renewable energies (*e.g.* wind, solar and tidal) are rapidly gaining ground, but suffer from intermittency issues.[6] Chemical fuels produced from renewable energy are regarded as an effective energy storage strategy; renewable energy is stored in periods of availability and low demand, to be used in periods of low supply and high demand.[7] Hydrogen gas, H_2, is a versatile chemical fuel, which can be used as a solar fuel when produced via renewables-driven electrolysis.[8–10] Electrochemical water splitting is composed of two half reactions: the hydrogen evolution reaction (HER) and the oxygen evolution reaction (OER).[11,12] The HER is the cathodic (reduction) reaction, is well studied, and can be done with little overpotential.[11,12]

$$2\,H_2O(l) \longrightarrow 2\,H_2(g) + O_2(g) \qquad \text{(overall)}$$

$$4\,H_2O(aq) + 4\,e^- \longrightarrow 2\,H_2(g) + 4\,OH^-(aq) \qquad \text{(HER)}$$

$$4\,OH^-(aq) \longrightarrow O_2(g) + 2\,H_2O(l) + 4\,e^- \qquad \text{(OER)}$$

While H_2 is the fuel of interest, the OER is recognized as the major bottleneck for H_2 pro-

duction as it is thermodynamically and kinetically challenging. It includes multiple proton-coupled electron transfers and an oxygen-oxygen bond formation.[13] While the HER involves a single intermediate, the OER requires the formation of three surface-adsorbed intermediates. Each of these intermediate formation steps happen individually, as multiple electron transfer steps at one time is not kinetically likely, resulting in sluggish OER kinetics and a large overpotential.[10–12,14,15] As such, potent catalysts are required for this reaction to be driven at an appreciable rate. The large-scale deployment of energy storage requires fundamental improvements in the catalysts employed.

Noble metal-based materials are often regarded as benchmark electrocatalysts for the OER. Of these, Ru and and Ir oxides have emerged as the most promising in both alkaline and acididc electrolyte. Reier *et al.* presented a comparative study of the activity and stability of acidic OER over oxidized Ru, Ir, and Pt nanoparticles.[16] The study found the catalytic activity to decrease in the order of Ru > Ir > and Pt. Despite remarkable OER performance by Ru, it succumbs to corrosion at applied potentials and was therefore incapable of sustaining such activity. Aside from the high cost and low abundance of these precious metals, this study highlights the Achilles heel of these high-performing catalysts, their stability under OER conditions. Ir finds relatively good OER stability. However, at high anodic potentials, dissolution has been reported to occur by the formation of Ir^{6+} species. The instability of Ru has been reported to arise due to the formation of soluble high oxidation states of RuO_2. Anodic polarization of the $Ru^{4+}O_2$ electrode produces a volatile tetroxide $Ru^{8+}O_4$, resulting in the dissolution of the Ru active site.

Our group has pioneered the use of UV-driven photochemical deposition to produce amorphous metal oxy(hydroxide) OER catalysts.[17] Many times, we have found that amorphous catalysts outperform otherwise identical crystalline variants,[17,18] including IrO_x.[19] Similarly, Salvatore *et al.* produced RuO_2 OER catalysts[20] from the photo decomposition of $(tmhd)_2COD$ based organometallic complexes.[21] However, $Ru(tmhd)_2COD$ derived photodeposited films were not characterized due to poor adhesion to substrate.[20] A simple solution to this limitation was to produce RuO_2 thin films using inorganic precursors treated with near infrared light, a method

called near infrared driven decomposition (NIRDD).[20,22] In general, both photodeposition approaches provide scalable, low-cost avenues to producing amorphous metal (oxy)hydroxides.

The enhanced catalytic performance of these amorphous materials however remains largely unexplained. X-ray absorption spectroscopy had proven to be an invaluable tool in resolving mechanistic aspects of the OER mediated by these photodeposited materials; however such studies have to date focused on first-row transition metal-based materials.[23–26]

In this work we structurally, spectroscopically and electrochemically investigate ruthenium oxide films produced by both photochemical methods (UV-driven and NIRDD) to determine the effect of the synthetic route on the catalytic activity of RuO_x electrocatalysts under alkaline conditions. Our main findings are that the deposition method has a significant impact on structure, electrocatalytic performance and durability, while the precursor used does not appear to have much influence. Specifically, using a combination of x-ray photoelectron spectroscopy, electrochemical measurements, and XAS – including *in operando* methods – we find that the nanocrystalline NIR-deposited RuO_2 is the superior catalyst. Importantly, this nano-RuO_x electrocalyst is stable under alkaline conditions.

2 Results

Three photodeposited RuO_x electrocatalysts were evaluated in this study. Catalysts prepared under UV irradiation from ruthenium(II) 2-ethylhexanoate are labelled as $\mathbf{Ru^{UV}_{2eh}}$. Catalysts prepared under NIR light were made using two different precursors: ruthenium(II) 2-ethylhexanoate (labelled $\mathbf{Ru^{NIR}_{2eh}}$), and ruthenium(III) chloride hydrate (labelled $\mathbf{Ru^{NIR}_{Cl}}$).

2.1 IR study of the photodecomposition of the ruthenium 2-ethylhexanoate

A ruthenium precursor was synthesised starting with $RuCl_3 \cdot H_2O$ through a simple ligand exchange with 2-ethylhexanoic acid, and was found to have suitable UV absorption in the 230-260 nm range (see section S2.1 of the Supplementary Material). We investigated the photodecomposition of this precursor under UV light through FTIR spectroscopy (Fig. S3). While the

bands do not decrease in a monotonic manner – an indication that intermediate species are formed and further decomposed during the process – all bands are seen to decrease to the baseline within 8 hours. Similarly, this precursor also decomposes when exposed to NIR radiation (Fig. S4), in a significantly faster process as bands associated with the precursor are completely gone within an hour.

2.2 Structural characterization of the as-prepared RuO_x thin films

Fig. 1 shows the XRD patterns of $\mathbf{Ru_{2eh}^{NIR}}$, $\mathbf{Ru_{Cl}^{NIR}}$, and $\mathbf{Ru_{2eh}^{UV}}$ prepared on carbon paper. No Bragg reflections assigned to RuO_2 are observed for the $\mathbf{Ru_{2eh}^{UV}}$ film. The only discernible peaks observed for $\mathbf{Ru_{2eh}^{UV}}$ arise from the carbon paper substrate. This is consistent with the formation of an x-ray amorphous sample. In contrast, diffractograms for samples prepared by NIR irradiation (*i.e.*, $\mathbf{Ru_{2eh}^{NIR}}$ and $\mathbf{Ru_{Cl}^{NIR}}$) exhibit low-intensity, broad peaks at 26°, 35°, 40°, and 57°; peaks attributed to the RuO_2 (110), (101), (200), and (220) planes, respectively. The crystallite size of the NIRDD samples can be calculated *via* the Scherrer equation (Eqn. S1). A crystal size of 12.4 ± 1.3 and 17.70 ± 1.8 nm was estimated for $\mathbf{Ru_{2eh}^{NIR}}$ and $\mathbf{Ru_{Cl}^{NIR}}$, respectively.

The surface morphology of the deposited films was investigated by SEM. As can be observed in the images (Fig. S5), all three RuO_x samples maintained the fibrous texture of the carbon paper. However, NIR photodeposition produces a rough surface coating on the fibres (Fig. S5 (a-b) and (d-e)). In contrast, a smooth, featureless coating is obtained by UV-deposition.

XPS spectra of the as-prepared films were recorded and fit (Figs. 2 and S6-S8). Tables S1 and S2 compile all peak fitting parameters and assignments for the C 1s, Ru 3d and 3p, and O 1s core levels. The C 1s signal overlaps with the Ru 3d regions, and the resulting spectra is fit using two sets of spin-orbit split doublets for Ru 3d and their corresponding satellite peaks, and a single C 1s peak (Fig. 2). The Ru 3p region exhibits a spin-orbit split $3p_{3/2}$ and $3p_{1/2}$ doublet, and their accompanying satellites (Fig. S6). Within the O 1s spectra (Fig. S7), the main O 1s peak is assigned to the signal at 528.9 eV with a satellite at 530.1 eV. The presence of Cl is observed in the $\mathbf{Ru_{Cl}^{NIR}}$ survey spectra presented in Fig. S8.

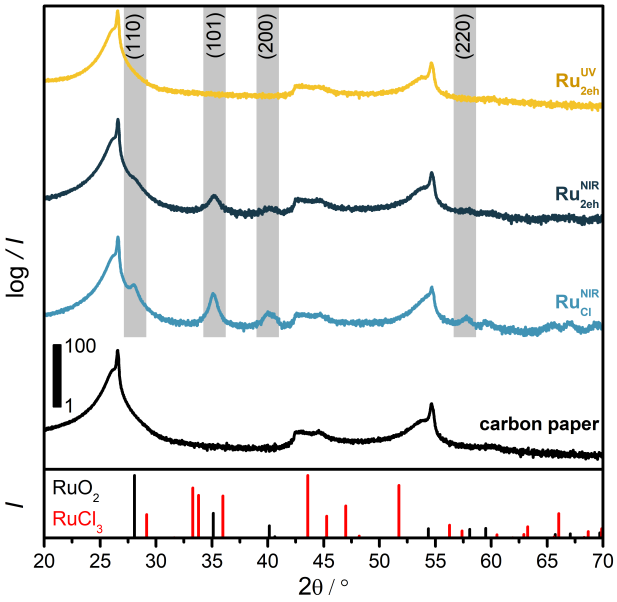

Figure 1: Powder XRD patterns collected on carbon paper, showing the RuO_x prepared by NIR are nanocrystaline (highlighted areas show Bragg peaks for RuO_2), while the UV-prepared sample is X-ray amorphous. Reference patterns are shown for $RuCl_3$ (ICSD ref n. 414040) and RuO_2 (ICSD ref no. 15071). Note that the experimental patterns are presented on a log scale as the carbon paper substrate peaks are significantly more intense than the RuO_x thin films, and offset for clarity.

X-ray absorption near edge structure (XANES) and extended X-ray absorption fine structure (EXAFS) probe the oxidation state and local structure environment at the Ru *K*-edge. The XANES spectra for the $\mathbf{Ru^{NIR}_{Cl}}$, $\mathbf{Ru^{NIR}_{2eh}}$, and $\mathbf{Ru^{UV}_{2eh}}$ samples are presented in Fig. 3a, along with a crystalline RuO_2 standard. To calibrate the XAS spectra, three reference compounds were also measured (Ru, $RuCl_3$, and RuO_2, with formal oxidation states of 0, +3, and +4, see Fig. S9). The resulting calibration curve showed that a positive *K*-edge position shift of ~0.795 eV is associated with a change in oxidation state of +1. We note that this number is lower than many estimates found in the literature, where shifts ranging from 1.16 to 1.91 eV per oxidation state are reported,[27–29] indicating our estimated oxidation states are likely to be taken as a upper limit. This difference may be due to the standard samples being used, the method used to determien the edge position, or a combination of both. With this in mind, when the *K*-edge positions of the $\mathbf{Ru^{NIR}_{Cl}}$, $\mathbf{Ru^{NIR}_{2eh}}$, $\mathbf{Ru^{UV}_{2eh}}$ are added to this curve, oxidation states can be inferred, with $\mathbf{Ru^{NIR}_{2eh}}$ showing an average Ru oxidation state of +6.1, $\mathbf{Ru^{NIR}_{Cl}}$ with +4.6, and $\mathbf{Ru^{UV}_{2eh}}$ having

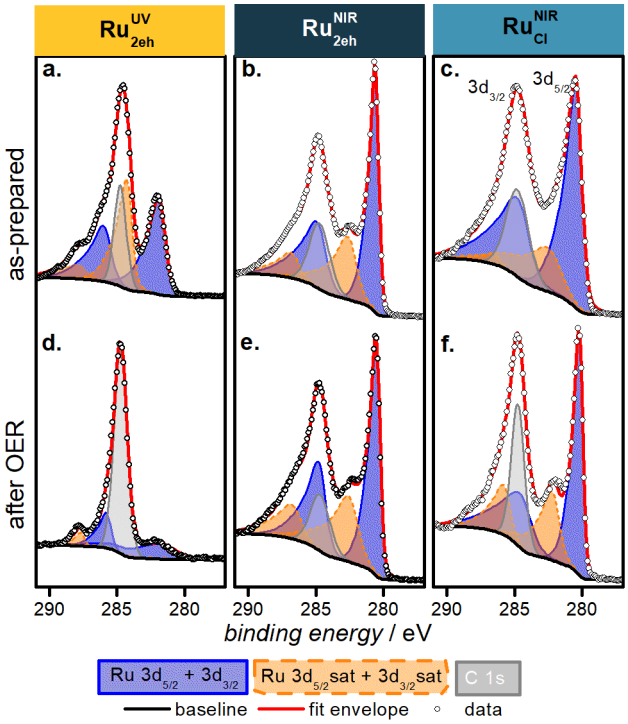

Figure 2: Ru 3d and C 1s XPS spectra for the $\mathbf{Ru}_{\mathbf{Cl}}^{\mathbf{NIR}}$, $\mathbf{Ru}_{\mathbf{2eh}}^{\mathbf{NIR}}$, and $\mathbf{Ru}_{\mathbf{2eh}}^{\mathbf{UV}}$ films. (a-c) are as-prepared, and (d-f) show samples after OER. In particular, note the significant decrease of the Ru 3d signal for the $\mathbf{Ru}_{\mathbf{2eh}}^{\mathbf{UV}}$ post-OER sample (d).

the lowest resting oxidation state of +3.5, noting the energy spanned by the 3 samples (2 eV) may correspond to a difference in oxidation state as small as ~ 1.05.

The EXAFS spectrum for $\mathbf{Ru}_{\mathbf{2eh}}^{\mathbf{UV}}$ is presented in Fig. 3b. Upon comparison with the crystalline RuO_2 standard it is clear the structural coherence is suppressed, as only a single peak near R = 1.98 Å is observed (Table S4). This lack of structural coherence is confirmed by the best fit (Table S3), which is based on rutile-phase RuO_2 ($P4_2/mnm$).[30] The prominent peak is assigned to a slightly distorted RuO_6 octahedron. Although the ratio between the equatorial and axial Ru-O bond distances remain the same as the crystalline counterpart (*i.e.*, 3% of extension), the overall RuO_2 structural framework of $\mathbf{Ru}_{\mathbf{2eh}}^{\mathbf{UV}}$ is relatively loose, with most fit bond distances being elongated. The fitting indicates all neighbouring Ru shells are drastically suppressed. This is consistent with the x-ray diffraction results, and an amorphous RuO_2 material, *a*-RuO_2. This behaviour has been observed in similar amorphous photodeposited metal (oxy)hydroxides thin films.[23,24,31] The coordination numbers for outer shells bonding are all lower than the crys-

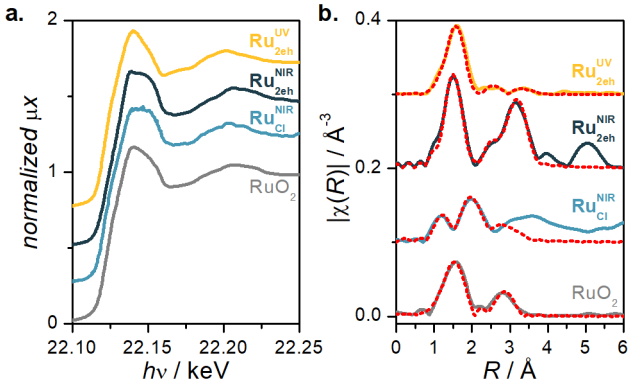

Figure 3: Ru K-edge XANES (a) and k^2-weighted $\chi(R)$ EXAFS spectra (b) of all three photodeposited samples, and crystalline RuO_2 as a reference compound. Red dotted lines are best fits to the data; spectra are offset for clarity.the sampels are well modelled with a rutile-phase RuO_2 ($P4_2/mnm$).

talline model compound; the Ru-Ru path for corner-sharing RuO_6 octahedra is shortened. This effect likely can be attributed to the displacement of surface RuO_6 octahedron from their ideal positions towards the surface of RuO_2 nanoparticles.

The XANES spectrum recorded for both NIR-deposited samples are very similar to that of RuO_2; in particular all three cases possess white line with a double-peak feature, however the relative intensities of these two peaks are all different. To elucidate the origin of this trend, we performed *ab initio* calculations using the FDMNES code[32] to simulate the X-ray absorption spectra of RuO_n clusters of different size (see Fig. S10). Modeling reveals a positive slope for the dual-peak white line shape for particles ranging in size from a RuO_6 octahedron up to particles with a 4.0 Å radius; a negative slope is observed for sizes > 4 Å to 6.0 Å. A change in relative intensity is reproduced by these calculations, indicating it could be related to particle size.

The EXAFS fit results for $\mathbf{Ru_{2eh}^{NIR}}$ are presented in Table S5. The local structural environment around the Ru atoms matches very well to that of RuO_2 of the $P4_2/mnm$ type.[30] The first coordination shell shows a slightly enhanced local structural distortion of the RuO_6 octahedron, when compared to what was reported by Goldschmidt.[30] The axial Ru-O bond along the 4-fold rotation axis is elongated by 0.03 Å, concomitant with the shortening of the four equatorial Ru-O bonds from 1.976 to 1.95 Å. The first shell structural distortions further impact the outer-shell Ru coordination environment accordingly.

The overall Ru local structure environment for $\mathbf{Ru}_{\mathbf{2eh}}^{\mathbf{NIR}}$ is the same as that of $\mathbf{Ru}_{\mathbf{2eh}}^{\mathbf{UV}}$, but more ordered (Table S5).

As was pointed out from XPS results, the presence of Cl was detected in our $\mathbf{Ru}_{\mathbf{Cl}}^{\mathbf{NIR}}$ sample. This is presumably unreacted $RuCl_3$, our starting material. The presence of $RuCl_3$ is confirmed from both the XANES and EXAFS analyses. Linear combination fitting of RuO_2 and $RuCl_3$ adequately reproduced the XANES spectrum, and its first derivative (see Fig. S11 and Table S6). Similarly, the EXAFS spectrum is appropriately fit by including both species (Table S7). The structural parameters extracted for RuO_2 indicated distances of 1.92, 2.06, and 3.22 Å for the equatorial Ru-O, axial Ru-O, and second-shell Ru-Ru bonds, respectively.

2.3 Electrochemistry

The electrocatalytic performance of the RuO_2 thin films was evaluated using a three-electrode system in 0.1 M KOH electrolyte. Measured cyclic voltammograms (CVs) are plotted in Fig. 4. All reported CVs are recorded after a minimum of 100 cycles at a scan speed of 0.01 V s^{-1} (see Fig. S13). As is shown in Fig. 4a, all three photodeposited samples exhibit a distinct anodic redox peak located at potentials 1.38 V, 1.38 V, and 1.77 V, for $\mathbf{Ru}_{\mathbf{Cl}}^{\mathbf{NIR}}$, $\mathbf{Ru}_{\mathbf{2eh}}^{\mathbf{NIR}}$, and $\mathbf{Ru}_{\mathbf{2eh}}^{\mathbf{UV}}$, respectively. To explore the reversibility of the catalyst, we also report the cathodic scan. The redox features of Ru appear to be reversible as the peaks are present in both the forward (anodic) and reverse (cathodic) sweep regions.

To benchmark the catalytic performance of the RuO_x catalysts, the Tafel slopes and overpotentials at catalytic onset η_{onset}, and 10 mA cm^{-2} were determined (Table 1). Nominal differences in catalytic activity were found amongst the NIR-deposited samples, indicating little dependence on the metal precursor used in deposition. Moreover, OER activity over the $\mathbf{Ru}_{\mathbf{Cl}}^{\mathbf{NIR}}$ and $\mathbf{Ru}_{\mathbf{2eh}}^{\mathbf{NIR}}$ electrocatalysts is in-line with previously reported RuO_x materials.[33–37] The $\mathbf{Ru}_{\mathbf{2eh}}^{\mathbf{UV}}$ catalyst, on the other hand, presented markedly different OER performance. All benchmarking parameters were significantly higher for $\mathbf{Ru}_{\mathbf{2eh}}^{\mathbf{UV}}$ when contrasted against $\mathbf{Ru}_{\mathbf{Cl}}^{\mathbf{NIR}}$ and $\mathbf{Ru}_{\mathbf{2eh}}^{\mathbf{NIR}}$ (Table 1).

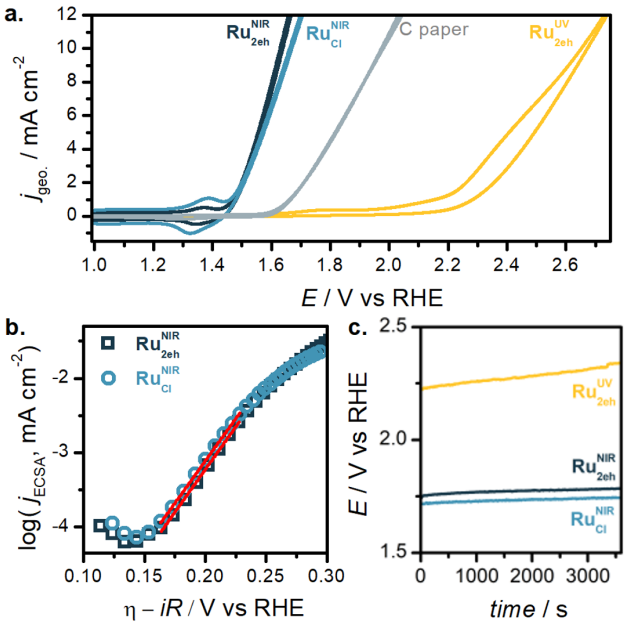

Figure 4: Electrochemical characterization of the RuO_x electrocatalysts in 0.1 M KOH electrolyte. a. Cyclic voltammograms normalized to geometric surface area, b. Tafel plots, c. chronoamperometry. As can be seen, there is little difference between the nanocrystalline NIR-deposited samples, which greatly outperform the UV-deposited sample.

Chronopotentiometry experiments were carried out to probe the stability of the RuO_x catalysts during the first hour of operation (Fig. 4c). At a current density of 10 mA cm^{-2}, $\mathbf{Ru^{NIR}_{Cl}}$ and $\mathbf{Ru^{NIR}_{2eh}}$ showed good stability with only about a 3 % increase in potential after one hour. On the contrary, $\mathbf{Ru^{UV}_{2eh}}$ exhibits poor stability, with roughly a 9 % potential increase within the same one-hour window.

Table 1: Kinetic paramters for RuOx thin films

Sample	Tafel slope (mV dec^{-1}))	η_{onset} (V)	$\eta_{10\,mA\,cm^{-2}}$ (V)
$\mathbf{Ru^{NIR}_{2eh}}$	44	0.15	0.40
$\mathbf{Ru^{NIR}_{Cl}}$	43	0.15	0.43
$\mathbf{Ru^{UV}_{2eh}}$	220	0.76	1.42

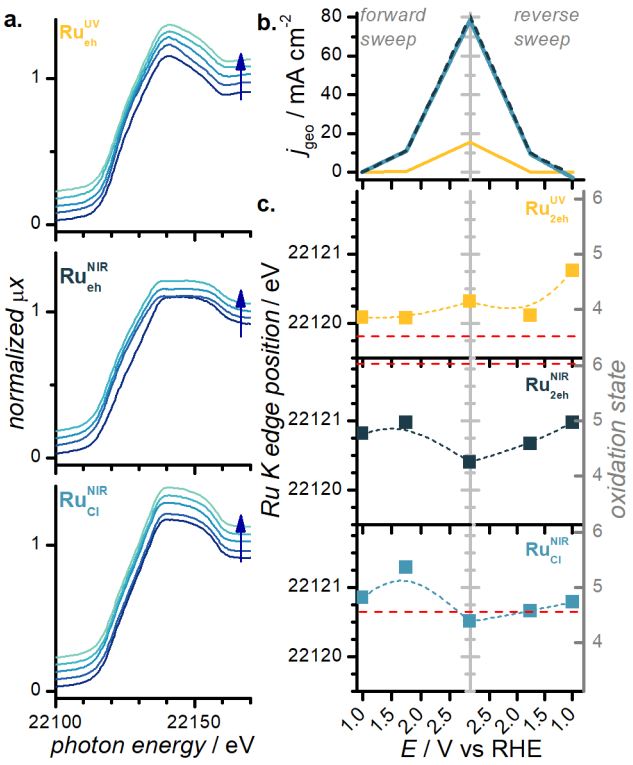

Figure 5: *Operando* XANES spectra for the three photodeposited RuO_2 samples (a) as the potential E is applied (b). The K edge position is presented as a function of E. A potential of 0.99, 1.75, and 2.85 V vs RHE is applied for steps 1 & 5, 2 & 4, and 5, respectively. The dashed horizontal lines in (c) are the *ex situ* edge positions.

2.4 *In-* and *post-operando* characterization

The XRD patterns of the *post operando* $\mathbf{Ru_{Cl}^{NIR}}$ and $\mathbf{Ru_{2eh}^{NIR}}$ are shown in Fig. S15. No new phases were observed. However, Scherrer analysis revealed an increase in crystallite size after OER. Crystallite size in the $\mathbf{Ru_{Cl}^{NIR}}$ increased from 17.70 ± 1.8 nm to 22.65 ± 2.4 nm, whereas the $\mathbf{Ru_{2eh}^{NIR}}$ crystallite grew from 12.4 nm ± 1.3 to 19.6 ± 2.1 nm post-OER. *Post operando* XRD analysis of the $\mathbf{Ru_{2eh}^{UV}}$showed that its amorphous phase was preserved throughout operation.

The XPS spectra before and after OER operation are shown in Fig. 2, S6 and S7 ($\mathbf{Ru_{2eh}^{UV}}$**–PO**, $\mathbf{Ru_{2eh}^{NIR}}$**–PO**, $\mathbf{Ru_{Cl}^{NIR}}$**–PO**)

The intensity of the Ru 3d core level spectra greatly decreases in the $\mathbf{Ru_{2eh}^{UV}}$**–PO** spectra (Fig. 2d). The $3d_{5/2}$ and $3d_{3/2}$ peaks after operation shift down by 0.1-0.2eV to 281.5 and 285.7 eV, respectively. After operation, the $3d_{5/2}$ satellite peak was not resolved. Within the Ru 3p region shown in Fig. S6, only the SnO substrate was resolved, indicating that the film deteriorated during operation. The $\mathbf{Ru_{2eh}^{NIR}}$**–PO** XPS spectra before and after operation is shown in Fig. 2b & e. Ru $3d_{5/2}$, $3d_{3/2}$ barely change pre/post OER. The Ru 3p spectra shown in Fig. S6 display identical peak positions pre and post-operation. The O 1s has an anhydrous peak present in both the as-prepared and in the post-operation; however the peak becomes sharper and higher in intensity, with the FWHM decreasing from 3.09 to 2.91 eV.

Fig. 2 shows the $\mathbf{Ru_{Cl}^{NIR}}$ spectra before and after OER operation ($\mathbf{Ru_{Cl}^{NIR}}$**–PO**). The $\mathbf{Ru_{Cl}^{NIR}}$**–PO** shifts to lower binding energy, with main Ru $3d_{5/2}$ and $3d_{3/2}$ peaks centered at 280.1 and 284.3 eV, respectively. This 0.2 eV downward shift (also observed in the O 1s spectra, Fig. S7) is indicative of a change in hydration, and agrees with literature results.[38] The Ru 3p spectra (Fig. S6) also exhibits a decrease in binding energy of the peaks after operation. An additional O 1s peak appears at 532 eV post-OER, assigned to an anhydrous oxide.

The *operando* XAS measurements were conducted to investigate the changing ruthenium oxide catalyst as a function of applied potential, during and after a catalytic cycle (Fig. 5).

The $\mathbf{Ru_{2eh}^{UV}}$ Ru K edge spectrum showed little variation in oxidation state throughout the potential cycle, the edge shifting by 0.68 eV from OCP to the highest potential reached. The

largest change happens as the catalyst returns back down to OCP, resting at $Ru^{4.7+}$ after operation. $\mathbf{Ru_{Cl}^{NIR}}$ and $\mathbf{Ru_{2eh}^{NIR}}$ follow similar general trends, first increasing, before reaching their lowest state under OER conditons, and coming back close to its initial state.

3 Discussion

To gain insights into the OER over the photodeposited RuO_x catalysts, we first look at their electrochemical performance. Polarization curves of the $\mathbf{Ru_{2eh}^{UV}}$, $\mathbf{Ru_{2eh}^{NIR}}$, $\mathbf{Ru_{Cl}^{NIR}}$, and bare C-paper are displayed in Fig. 4. Using the CVs to evaluate the overall OER activity, the NIR-deposited samples clearly outperform the $\mathbf{Ru_{2eh}^{UV}}$, following the order: $\mathbf{Ru_{Cl}^{NIR}} \approx \mathbf{Ru_{2eh}^{NIR}} > \mathbf{Ru_{2eh}^{UV}}$. Preceding the onset of the OER, a distinct, reversible, peak at roughly 1.375 V vs RHE corresponding to the Ru(VI/VII) redox couple is observed in both the $\mathbf{Ru_{Cl}^{NIR}}$ and $\mathbf{Ru_{2eh}^{NIR}}$ samples.[39–41] A much less prominent peak is seen in the $\mathbf{Ru_{2eh}^{UV}}$ sample at a higher potentials of 1.781 V vs RHE. This redox peak has been previously used to contrast the activity of different RuO_2 catalysts, where it was found that the integrated charge of the anodic peak scales with OER activity.[39] In other words, the greater the charge discernible from the integration of the anodic Ru(VI/VII) peak, the greater the catalytic activity of RuO_x. A greater charge was linked with the availability of unsaturated Ru active sites. This analysis of the Ru(VI/VII) redox peak is employed herein to distinguish amongst the similar OER activities of the NIR-formed catalysts. By varying the metal precursor in the photodeposition, we find a marginal increase in the $\mathbf{Ru_{Cl}^{NIR}}$ Ru(VI/VII) redox peak area relative to $\mathbf{Ru_{2eh}^{NIR}}$. As reported in literature, this suggests that a slightly greater number of oxidizable Ru-active sites are accessible by using the $RuCl_3$ precursor when compared to the ruthenium 2-ethylhexanoate precursor.

To elucidate any compositional effects of the RuO_x on the catalytic activity and remove any contributions by differences in surface area (i.e., morphology), the electrochemically active surface area (ECSA) was determined from the double-layer capacitance (C_{dl}).[42] In brief, CVs were obtained in a potential region of minimal faradaic current response at various scan rates. The only current contributor is assumed to be from the charging of the double layer. The slope of

the charging currents as a function of scan rate yields the C_{dl} (Fig. S12). The ECSA values calculated for $\mathbf{Ru}_{\mathbf{Cl}}^{\mathbf{NIR}}$ and $\mathbf{Ru}_{\mathbf{2eh}}^{\mathbf{NIR}}$ were 509 and 283 cm^2, respectively, per geometric cm^2. These ECSAs were two orders of magnitude higher than that of $\mathbf{Ru}_{\mathbf{2eh}}^{\mathbf{UV}}$ (1.76 cm^2). With these results, it can be deduced that the the nominally better electrocatalytic performance of $\mathbf{Ru}_{\mathbf{Cl}}^{\mathbf{NIR}}$ when compared to $\mathbf{Ru}_{\mathbf{2eh}}^{\mathbf{NIR}}$ likely arises from a higher ECSA. However, the ECSA results fail to explain the sluggish kinetics of the $\mathbf{Ru}_{\mathbf{2eh}}^{\mathbf{UV}}$.

Activity descriptors were attained to further explore the differences amongst the prepared RuO_x catalysts. Namely, we report the minimum potential required to produce O_2 (η_{onset}), and the overpotentials η, required to reach a current density of 10 mA cm^{-2} (Table 1). In-line with the results discussed above, the electrochemical activities of the NIR-deposited films are virtually identical to one another. Predominantly, the differences arise when the catalyst preparation method is altered. An η_{onset} of 0.15 V vs RHE was obtained with the $\mathbf{Ru}_{\mathbf{Cl}}^{\mathbf{NIR}}$ and $\mathbf{Ru}_{\mathbf{2eh}}^{\mathbf{NIR}}$, whereas a significantly higher 0.76 V vs RHE was observed for $\mathbf{Ru}_{\mathbf{2eh}}^{\mathbf{UV}}$.

The steady-state Tafel slope measurements of the RuO_x catalysts were carried out to gain a better understanding of the kinetics at play. Tafel slopes are determined from the linear regions in Fig. 4b, and reported in Table 1. The Tafel slope is a kinetic parameter, correlated to the rate-determining step of the OER. Further, the slope is often used as a phenomenological descriptor of catalytic activity, indicating the overpotential increase required to raise the current density (*i.e.*, rate) by one order of magnitude. As expected from the results discussed above, the NIR-prepared samples show near equivalent Tafel behaviours with slopes of 44 and 43 mV dec^{-1} for the $\mathbf{Ru}_{\mathbf{2eh}}^{\mathbf{NIR}}$ and $\mathbf{Ru}_{\mathbf{Cl}}^{\mathbf{NIR}}$, respectively. A slope nearing 40 mV dec^{-1} suggests a second electron transfer to limit the overall rate of the reaction.[43] On the other hand, a large slope of 220 mV dec^{-1} was obtained for $\mathbf{Ru}_{\mathbf{2eh}}^{\mathbf{UV}}$. Such a dramatic increase in Tafel slope, compared to the NIR-formed catalysts, evince the hampered OER kinetics over the amorphous catalyst. Notably, 220 mV dec^{-1} significantly deviates from the commonly reported Tafel slopes for simple OER electron-transfer reactions, 120, 60, 40, 15 mV dec^{-1}.[43,44] Various rationales for anomalously high Tafel slopes have been proposed. Particularly, potential drops throughout the catalyst due

to factors such as large thickness variations and formation of poorly conductive (high ohmic resistance) layers.[45,46] This causes a potential distribution through the catalysts and can lead to low values of the charge transfer coefficient α (< 0.5). Decreasing the value of α by half, the Tafel slope is subsequently doubled. Another common explanation for the stark increase in the Tafel slope is the change of adsorbed species surface coverage.[39,47] This effect is especially true at higher overpotentials, where the dominant surface termination of noble metal oxides has been reported to evolve from a hydroxy to oxo groups, producing Tafel slopes of 240 mV dec^{-1}.[47] Assuming a doubling of the Tafel slope (α value halved) by the amorphous $\mathbf{Ru}_{\mathbf{2eh}}^{\mathbf{UV}}$ electrode, the OER is limited by the first electron-transfer step; commonly ascribed to a 120 mV dec^{-1} slope.[44]

The catalytic stability of the photodeposited samples in alkaline conditions was characterized by chronopotentiometry. The analysis revealed yet another clear advantage of the NIRDD technique over the UV-deposited as it relates to RuO_x catalysts. Only a 3 % activity loss was observed during the first hour of operating the $\mathbf{Ru}_{\mathbf{Cl}}^{\mathbf{NIR}}$ and the $\mathbf{Ru}_{\mathbf{2eh}}^{\mathbf{NIR}}$ at 10 mA cm^{-2}, whereas 9 % was observed in the $\mathbf{Ru}_{\mathbf{2eh}}^{\mathbf{UV}}$. The Pourbaix diagram of RuO_2 sheds some light into its instability: above a pH of 12, Ru will form soluble species at even modest potentials.[48] Stability issues experienced with Ru-based electrocatalysts are attributed to the formation of higher oxidation states of the oxide by an applied anodic potential (e.g., $RuO_2 \rightarrow RuO_4$).[49,50] Consequently, dissolution of the RuO_4 diminishes OER activity. In our case, it appears the nanocrystalline phase imparts additional stability to the material, even at pH = 13. The amorphous phase does not convey this desirable added stability. To enhance the stability of Ru-based electrocatalysts, various strategies such as heteroatom doping and nanostructuring have been employed. However, few reports show stable RuO_x catalysts in alkaline conditions. Our results indicate that a highly stable alkaline OER RuO_x catalyst can be accessed through the NIRDD method. Accordingly, this emphasizes the importance of the deposition method utilized in preparation of the catalyst, while the Ru precursor seems to have little-to-no impact on catalysts performance.

To place our results in-context with that reported in literature, the η (10 mA cm^{-2}) of various noble metal (Ir and Ru) based alkaline OER catalysts is plotted in Fig. S14.[34,36,51–57] The NIR-

prepared catalysts are within the expected activity range, especially when compared to RuO_2. On the other hand, the UV-deposited sample exhibits strikingly poor activity, relative to those reported. Intriguingly, throughout our investigations of photodeposited amorphous OER catalysts, we have previously found the general trend that the amorphous OER electrocatalysts outperform their crystalline counterpart.[17,19,23,24,58,59] In this case, we find that the amorphous material is neither performing, or durable. In contrast, the nanocrystalline RuO_x presents excellent stability under alkaline conditions.

To date, the stability of disordered OER catalyst materials remains a controversial topic within the literature. For instance, studies such as that conducted by Geiger *et al.*, show a general trend of increasing activity but decreasing stability when transitioning from an ordered (crystalline) IrO_2 to the disordered (amorphous) phase.[60] This trend is also observed beyond the noble metals, in first-row transition metals.[61–63] Conversely, studies by Cherevko *et al.* and Jovanovič et al. suggest the opposite, where dissolution of IrO_2 is minimized by utilizing its amorphous phase.[64,65] These results suggest that, alike those obtained by $\mathbf{Ru_{Cl}^{NIR}}$, $\mathbf{Ru_{2eh}^{NIR}}$, and $\mathbf{Ru_{2eh}^{UV}}$, different types of disordered phases can be obtained. As we demonstrate, the deposition method is crucial in obtaining a disordered structure with desired stability and activity.

We now turn to correlating the electrocatalytic activity with structural features of the photodeposited films. By XRD, the NIRDD formed nanocrystalline phases of RuO_x, regardless of the metal precursor used. This is in good agreements with previous reports.[20] From the Scherrer estimation of the crystallite size slightly greater ordered domains are inferred for the $\mathbf{Ru_{Cl}^{NIR}}$ over the $\mathbf{Ru_{2eh}^{NIR}}$. On the other hand, the UV-deposited sample was found to be fully XRD-amorphous, as is typical of the UV photodeposition method.[17,19,23,24,31]

The Ru 3d core level spectra are useful to differentiate between anhydrous RuO_2 and hydrated $RuO_2 \cdot xH_2O$; the latter having wider peaks (as evidenced from larger FWHM) and suppressed satellite peaks when compared to anhydrous RuO_2.[38,66] However, Morgan's study does not disentangle whether the hydration state or the crystallinity of the sample affects the spectrum more, which throws some ambiguity in our own interpretation that follows.[38]

Fig. 2a-c shows the Ru 3d XPS spectra for each of the RuO_x catalysts. In general, all samples show substantial satellite peaks, more consistent with RuO_2 than its hydrated counterpart.[38] Given we have amorphous and nanocrystalline species, in this size range it appears that the hydration level may indeed impact the spectrum more than crystallinity. The overall envelope of the $\mathbf{Ru_{2eh}^{UV}}$ sample displays different features compared to the $\mathbf{Ru_{2eh}^{NIR}}$ and $\mathbf{Ru_{Cl}^{NIR}}$ samples. $\mathbf{Ru_{2eh}^{UV}}$ has broader spectral features, which may indicate more atomic sites, or higher levels of hydration; both being consistent with its amorphous nature, and in agreement with our XRD and EXAFS analysis. The $\mathbf{Ru_{2eh}^{NIR}}$ has a high ratio of satellite to main peak as well as narrower features (Table S2), indicating it may be less hydrated than $\mathbf{Ru_{Cl}^{NIR}}$. This is further supported by the O 1s spectra, where the envelope for $\mathbf{Ru_{2eh}^{NIR}}$ is characteristic of anhydrous RuO_2.[38]

The EXAFS analysis is in general agreement with the the XPS and XRD data in that the samples are well modelled as RuO_2, and an increase in ordering is observed between the UV- and NIR-prepared samples.

XPS showed changes after OER operation, indicating a modification for the structure and/or composition of the sample while carrying out the OER. After a potential is applied, the $\mathbf{Ru_{2eh}^{UV}}$–**PO** catalyst disintegrates, as is tracked through the Ru 3d and 3p spectra; in the latter region only the SnO substrate's Sn 3d signal is visible, with no Ru present (Fig. S6). This behaviour is consistent with the low stability and performance of the $\mathbf{Ru_{2eh}^{UV}}$ sample, which required high potentials and thus operated in a window where dissolved Ru species are formed. After OER operation, the $\mathbf{Ru_{Cl}^{NIR}}$ and $\mathbf{Ru_{2eh}^{NIR}}$ both move towards a more anhydrous nature.

Even though the $\mathbf{Ru_{2eh}^{UV}}$ sample demonstrated low stability, it is interesting to observe that throughout *in operando* measurements, there is a progressive ordering occuring, as seen from the mean RuO_2 cluster size (Fig. S16, determined from size-dependent linear combination fitting). This increase in coordination number of the two outer shell Ru-O is due to a progressive oxygen vacancy occupancy, leading to a development of a more complete RuO_2 structural environment as catalysis proceeds. This may suggest that careful conditioning of the UV-deposited may be possible to render a more durable catalyst.

The $\mathbf{Ru_{2eh}^{NIR}}$ XANES spectra do not substantially change during potential cycling. Upon inspection of the first derivative of the signal, a trend consistent with crystalline domain size decrase is observed (Fig. S17).

$\mathbf{Ru_{Cl}^{NIR}}$ *in operando* EXAFS fitting revealed that RuO_2 is a major species of the $\mathbf{Ru_{Cl}^{NIR}}$ system, contrary to the as-prepared samples which contained $RuCl_3$ and RuO_2. As catalysis proceeds, linear combination fitting of the XANES spectra did not indicate any progression in the sample composition, and indicated that the major species (85-95 %) is RuO_2 throughout the catalytic cycle. Comparison of $\mathbf{Ru_{Cl}^{NIR}}$ between FEFF modeling and experimental data revealed identical EXAFS between steps 3-5. From an EXAFS perspective, the Ru local structural environment is identical between these steps, indicating no major structural changes happening during catalysis.

The evolution of oxygen can be approached by two different mechanistic pathways. The first being a 2e- transfer reaction, involving the direct coupling of 2M-O intermediates to form O_2. The other pathway is comprised of 4 e- transfers, proceeding through a M-OOH intermediate which decomposes to produce O_2. Although both require consideration, the general consensus in literature is that the OER is a 4-step reaction, forming reaction intermediates M-OH, M-O, and M-OOH to generate O_2.[12,49] Understanding catalyst transformations during the OER would provide new avenues for catalyst improvement and development. To this end, changes to the RuO_x catalysts during the OER were established by monitoring variations in the XANES XAS region at electrode potentials, held at values preceding, during, and succeeding OER catalysis. Shifts in the XANES spectra to higher energies ($\epsilon_\circ$) translates to an increase in oxidation state, and *vice-versa*.

Commencing the *operando* study with an applied potential (1 V vs RHE) in step 1, a considerable oxidation state change occurred in the amorphous catalyst, compared to the *ex-situ* results. $\mathbf{Ru_{2eh}^{UV}}$ oxidation state decreased from +6.1 (*ex-situ)* to +3.8 in step 1, whereas minor oxidation state changes of 0.2 and 1.2 were observed for $\mathbf{Ru_{Cl}^{NIR}}$ and $\mathbf{Ru_{2eh}^{NIR}}$, respectively. Initial oxidation state changes are expected, given the catalyst is being submerged in an alkaline

electrolyte and small potentials are applied.[67] However, the drastic changes of the $\mathbf{Ru}_{\mathbf{2eh}}^{\mathbf{UV}}$ are beyond expected, rather it may be a demonstration of the instability of the amorphous RuO_x phase. Evidence of this instability is also seen in the XPS and chronopotentiometry results.

The potential applied to catalyst is then pushed into the catalytic region, at 1.7 and 2.8 V vs RHE for steps 2 and 3, respectively. Little change in the Ru oxidation state in the amorphous catalyst is observed. This is in-line with the electrochemical results, in which sluggish OER kinetics govern the $\mathbf{Ru}_{\mathbf{2eh}}^{\mathbf{UV}}$. The nanocrystalline $\mathbf{Ru}_{\mathbf{Cl}}^{\mathbf{NIR}}$ and $\mathbf{Ru}_{\mathbf{2eh}}^{\mathbf{NIR}}$ are both oxidized in step 2, and subsequently reduced in step 3. Although the decrease in Ru oxidation state during catalysis would appear counterintuitive for the catalysis of an oxidation reaction, it has been previously rationalized by Pedersen *et al.*[66] Using DFT calculations, they show that just prior to onset, the dominant surface termination of RuO_2 is O* (an O atom adsorbed onto an open active site *); explaining the increase in Ru oxidation state at step 2. The conversion of this O* to OOH* was found to be the rate-limiting step of the OER over RuO_2. However, once the potential to convert O* → OOH* is overcome, O_2 is readily evolved. Therefore, as the potential is increased, the O* surface coverage is decreased as it is converted to O_2, leading to a reduction of the Ru oxidation state.

To close the catalytic cycle, the potential is reversed (in the cathodic direction) to 1.7 (step 4) and ~1 V vs RHE (step 5), alike step 1 and 2. With this, the reversibility of the RuO_x catalyst can be probed. The nanocrystalline samples recuperate their original oxidation state at the end of the cycle (step 5). Conversely, the amorphous catalyst terminated the OER cycle at a higher oxidation state from what it started. These results further support the notion that the amorphous Ru catalyst formed by UV-deposition is considerably unstable, and the nanocrystalline phase by NIRDD is stable under alkaline OER conditions.

4 Conclusions

In this work, we evaluated three electrocatalysts prepared by two photochemical methods: UV-driven photodeposition from a ruthenium 2-ethylhexanoate precursor, and NIR-driven decom-

position from the same ruthenium 2-ethylhexanoate, and ruthenium chloride. We find that the UV- and NIR-derived samples differ in their structure – one being amorphous, the latter nanocrystalline – and their electrochemical performance. The amorphous, UV-deposited RuO_2 has poor electrode performance, and limited stability under alkaline conditions. The nanocrystalline samples, however, have good OER catalysis capabilities and are, more importantly, stable under alkaline conditions. This removes a hurdle to the widespread use of RuO_2 as an alkaline OER catalyst.

Author Information

Corresponding author

Simon Trudel – *Department of Chemistry and Institute for Quantum Science and Technology, University of Calgary, 2500 University Dr NW, Calgary, AB, Canada*; https://orcid.org/0000-0001-5757-2219; Email: trudels@ucalgary.ca

Authors

Katelynn M. Daly – *Department of Chemistry and Institute for Quantum Science and Technology, University of Calgary, 2500 University Dr NW, Calgary, AB, Canada*; https://orcid.org/0000-0001-5700-3315

Santiago Jimenez-Villegas – *Department of Chemistry and Institute for Quantum Science and Technology, University of Calgary, 2500 University Dr NW, Calgary, AB, Canada*; https://orcid.org/0000-0001-8950-2899

Benjamin Godwin – *Department of Chemistry and Institute for Quantum Science and Technology, University of Calgary, 2500 University Dr NW, Calgary, AB, Canada*

Martin A. W. Schoen – *Department of Chemistry and Institute for Quantum Science and Technology, University of Calgary, 2500 University Dr NW, Calgary, AB, Canada*

Oliver Calderon – *Department of Chemistry and Institute for Quantum Science and Technology, University of Calgary, 2500 University Dr NW, Calgary, AB, Canada*;https://orcid.org/0000-0002-3804-9542

Ning Chen – *Hard X-ray Micro-Analysis Beamline, Canadian Light Source, 44 Innovation Boulevard, Saskatoon, SK S7N 2V3, Canada*; https://orcid.org/0000-0002-1269-6119

Author contribution

ST, KMD, and SJV conceived the project; KMD, BG, and SJV characterized the materials; all authors assisted with XAS data acquisition and interpretation; all authors reviewed the manuscript.

Note

The authors declare no competing conflicts of interest.

Acknowledgement

The authors thank Natural Sciences and Engineering Research Council (NSERC) of Canada (Discovery Grant) for operating funds. This research used facilities funded by the University of Calgary (UofC) and the Canadian Foundation for Innovation (CFI) John R. Evans Leaders Fund. K.D. acknowledges funding from the Alberta Graduate Excellence Scholarship - Indigenous (UofC); S.J.V. acknowledges funding from the UofC's Global Research Initiative in Sustainable Low Carbon Unconventional Resources (GRI) funded by the Canada First Research Excellence Fund (CFREF); M.A.W.S. acknowledges funding from the Alexander von Humboldt Foundation Feodor Lynen Research Fellowship and the UofC's GRI funded by the CFREF; O.C. acknowledges funding from the UofC's GRI funded by the CFREF and the Nova Schemicals Scholarship (UofC). Part or all of the research described in this paper was performed at the Canadian Light Source, a national research facility of the University of Saskatchewan, which is supported by the CFI, NSERC, the National Research Council (NRC), the Canadian Institutes of Health Research (CIHR), the Government of Saskatchewan, and the University of Saskatchewan.

Supporting Information Available

Experimental procedures, methods, [17,18,20,38,58,68–82] and materials, including additional XS, XPS, electrochemistry, FTIR spectroscopy, and SEM micrographs.

References

(1) McKay, D. I. A.; Staal, A.; Abrams, J. F.; Winkelmann, R.; Sakschewski, B.; Loriani, S.; Fetzer, I.; Cornell, S. E.; Rockström, J.; Lenton, T. M. Exceeding 1.5 °C global warming could trigger multiple climate tipping points. *Science* **2022**, *377*, eabn7950.

(2) Edenhofer, O. *Mitigation of climate change*; Cambridge University Press, 2014.

(3) Hosseini, S. E.; Wahid, M. A. Hydrogen production from renewable and sustainable energy resources: Promising green energy carrier for clean development. *Renew. Sust. Energ. Rev.* **2016**, *57*, 850–866.

(4) De Cian, E.; Wing, I. S. Global energy consumption in a warming climate. *Environ. Resour. Econ.* **2019**, *72*, 365–410.

(5) Lewis, N. S.; Nocera, D. G. Powering the planet: Chemical challenges in solar energy utilization. *Proc. Natl. Acad. Sci. U.S.A.* **2006**, *103*, 15729–15735.

(6) Gowrisankaran, G.; Reynolds, S. S.; Samano, M. Intermittency and the value of renewable energy. *J. Polit. Econ.* **2016**, *124*, 1187–1234.

(7) Cook, T. R.; Dogutan, D. K.; Reece, S. Y.; Surendranath, Y.; Teets, T. S.; Nocera, D. G. Solar Energy Supply and Storage for the Legacy and Nonlegacy Worlds. *Chem. Rev.* **2010**, *110*, 6474–6502.

(8) Dincer, I. Renewable energy and sustainable development: a crucial review. *Renew. Sust. Energ. Rev.* **2000**, *4*, 157 – 175.

(9) Eriksson, E.; Gray, E. Optimization and integration of hybrid renewable energy hydrogen fuel cell energy systems – A critical review. *Appl. Energy* **2017**, *202*, 348 – 364.

(10) Kreuter, W.; Hofmann, H. Electrolysis: The important energy transformer in a world of sustainable energy. *Int. J. Hydrog. Energy* **1998**, *23*, 661 – 666.

(11) Wang, H.; Gao, L. Recent developments in electrochemical hydrogen evolution reaction. *Curr. Opin. Electrochem.* **2018**, *7*, 7 – 14.

(12) Suen, N.-T.; Hung, S.-F.; Quan, Q.; Zhang, N.; Xu, Y.-J.; Chen, H. M. Electrocatalysis for the oxygen evolution reaction: recent development and future perspectives. *Chem. Soc. Rev.* **2017**, *46*, 337–365.

(13) Gong, M.; Dai, H. A mini review of NiFe-based materials as highly active oxygen evolution reaction electrocatalysts. *Nano Research* **2015**, *8*, 23–39.

(14) Dau, H.; Limberg, C.; Reier, T.; Risch, M.; Roggan, S.; Strasser, P. The mechanism of water oxidation: from electrolysis via homogeneous to biological catalysis. *ChemCatChem* **2010**, *2*, 724–761.

(15) Kanan, M. W.; Nocera, D. G. In Situ Formation of an Oxygen-Evolving Catalyst in Neutral Water Containing Phosphate and Co^{2+}. *Science* **2008**, *321*, 1072–1075.

(16) Reier, T.; Oezaslan, M.; Strasser, P. Electrocatalytic oxygen evolution reaction (OER) on Ru, Ir, and Pt catalysts: a comparative study of nanoparticles and bulk materials. *ACS Catal.* **2012**, *2*, 1765–1772.

(17) Smith, R. D. L.; Prévot, M. S.; Fagan, R. D.; Zhang, Z.; Sedach, P. A.; Siu, M. K. J.; Trudel, S.; Berlinguette, C. P. Photochemical Route for Accessing Amorphous Metal Oxide Materials for Water Oxidation Catalysis. *Science* **2013**, *340*, 60–63.

(18) Zhang, C.; Berlinguette, C. P.; Trudel, S. Water oxidation catalysis: An amorphous quaternary Ba-Sr-Co-Fe oxide as a promising electrocatalyst for the oxygen-evolution reaction. *Chem. Commun.* **2016**, *52*, 1513–1516.

(19) Smith, R.; Sporinova, B.; Fagan, R.; Trudel, S.; Berlinguette, C. Facile photochemical preparation of amorphous iridium oxide films for water oxidation catalysis. *Chem. Mater.* **2014**, *26*, 1654–1659.

(20) Salvatore, D. A.; Peña, B.; Dettelbach, K. E.; Berlinguette, C. P. Photodeposited ruthenium dioxide films for oxygen evolution reaction electrocatalysis. *J. Mater. Chem. A* **2017**, *5*, 1575–1580.

(21) Guizhi, L.; Trudel, S.; Hill, R. H. Photolithographic Deposition of Ruthenium Thin Films By Photochemical Metal Organic Deposition. *J. Photopolym. Sci. Technol.* **2006**, *19*, 459–465.

(22) Salvatore, D. A.; Dettelbach, K. E.; Hudkins, J. R.; Berlinguette, C. P. Near-infrared–driven decomposition of metal precursors yields amorphous electrocatalytic films. *Sci. Adv.* **2015**, *1*, e1400215.

(23) Schoen, M. A. W.; Randell, N. M.; Calderon, O.; Jimenez Villegas, S.; Thomson, Z.; Chernikov, R.; Trudel, S. Structural Evolution in Photodeposited Nickel (oxy)hydroxide Oxygen Evolution Electrocatalysts. *ACS Appl. Energy Mater.* **2020**, *3*, 12407–12416.

(24) Schoen, M. A. W.; Calderon, O.; Randell, N. M.; Jimenez-Villegas, S.; Daly, K. M.; Chernikov, R.; Trudel, S. Local structural changes in polyamorphous (Ni,Fe)O_x electrocatalysts suggest a dual-site oxygen evolution reaction mechanism. *J. Mater. Chem. A* **2021**, *9*, 13252–13262.

(25) Smith, R. D. L.; Pasquini, C.; Loos, S.; Chernev, P.; Klingan, K.; Kubella, P.; Mohammadi, M. R.; González-Flores, D.; Dau, H. Spectroscopic identification of active sites for the oxygen evolution reaction on iron-cobalt oxides. *Nat. Commun.* **2017**, *8*, 2022.

(26) Smith, R. D. L.; Pasquini, C.; Loos, S.; Chernev, P.; Klingan, K.; Kubella, P.; Mohammadi, M. R.; González-Flores, D.; Dau, H. Geometric distortions in nickel (oxy)hydroxide electrocatalysts by redox inactive iron ions. *Energy Environ. Sci.* **2018**, *11*, 2476–2485.

(27) Hoque, M. A. et al. Water oxidation electrocatalysis using ruthenium coordination oligomers adsorbed on multiwalled carbon nanotubes. *Nat. Chem.* **2020**, *12*, 1060–1066.

(28) Hiley, C. I.; Lees, M. R.; Fisher, J. M.; Thompsett, D.; Agrestini, S.; Smith, R. I.; Walton, R. I. Ruthenium(V) Oxides from Low-Temperature Hydrothermal Synthesis. *Angew. Chem. Int. Ed.* **2014**, *53*, 4423–4427.

(29) Sardar, K.; Petrucco, E.; Hiley, C. I.; Sharman, J. D. B.; Wells, P. P.; Russell, A. E.; Kashtiban, R. J.; Sloan, J.; Walton, R. I. Water-Splitting Electrocatalysis in Acid Conditions Using Ruthenate-Iridate Pyrochlores. *Angew. Chem. Int. Ed.* **2014**, *53*, 10960–10964.

(30) Goldschmidt, V. Geochemische Verteilungsgesetze VII. Die Gesetze der Krystallochemie. *Skrifter utgitt av det Norske Videnskaps-Akademi i Oslo 1: Matematisk-Naturvidenskapelig Klasse* **1926**, *1926*, 1–117, Crystallographic Open Database # 1538150.

(31) Trudel, S.; Daryl Crozier, E.; Gordon, R. A.; Budnik, P. S.; Hill, R. H. X-ray absorption fine structure study of amorphous metal oxide thin films prepared by photochemical metalorganic deposition. *J. Solid State Chem.* **2011**, *184*, 1025–1035.

(32) Bunău, O.; Joly, Y. Self-consistent aspects of X-ray absorption calculations. *J. Condens. Matter Phys.* **2009**, *21*, 345501.

(33) Galani, S. M.; Mondal, A.; Srivastava, D. N.; Panda, A. B. Development of RuO_2/CeO_2 heterostructure as an efficient OER electrocatalyst for alkaline water splitting. *Int. J. Hydrog. Energy* **2020**, *45*, 18635–18644.

(34) Lu, X.; Sakai, N.; Tang, D.; Li, X.; Taniguchi, T.; Ma, R.; Sasaki, T. CoNiFe Layered Double Hydroxide/$RuO_{2.1}$ Nanosheet Superlattice as Carbon-Free Electrocatalysts for Water Splitting and Li–O_2 Batteries. *ACS Appl. Mater. Interfaces* **2020**, *12*, 33083–33093.

(35) Liyanage, D. R.; Li, D.; Cheek, Q. B.; Baydoun, H.; Brock, S. L. Synthesis and oxygen evolution reaction (OER) catalytic performance of $Ni_{2x}Ru_xP$ nanocrystals: enhancing activity by dilution of the noble metal. *J. Mater. Chem. A* **2017**, *5*, 17609–17618.

(36) Ding, J.; Shao, Q.; Feng, Y.; Huang, X. Ruthenium-nickel sandwiched nanoplates for efficient water splitting electrocatalysis. *Nano Energy* **2018**, *47*, 1–7.

(37) Ma, W.; Ma, R.; Wang, C.; Liang, J.; Liu, X.; Zhou, K.; Sasaki, T. A Superlattice of Alternately Stacked Ni–Fe Hydroxide Nanosheets and Graphene for Efficient Splitting of Water. *ACS Nano* **2015**, *9*, 1977–1984.

(38) Morgan, D. J. Resolving ruthenium: XPS studies of common ruthenium materials. *Surf. Interface Anal.* **2015**, *47*, 1072–1079.

(39) Stoerzinger, K. A.; Qiao, L.; Biegalski, M. D.; Shao-Horn, Y. Orientation-Dependent Oxygen Evolution Activities of Rutile IrO_2 and RuO_2. *J. Phys. Chem. Lett.* **2014**, *5*, 1636–1641.

(40) Doyle, R. L.; Godwin, I. J.; Brandon, M. P.; Lyons, M. E. G. Redox and electrochemical water splitting catalytic properties of hydrated metal oxide modified electrodes. *Phys. Chem. Chem. Phys.* **2013**, *15*, 13737–13783.

(41) Stoerzinger, K. A.; Rao, R. R.; Wang, X. R.; Hong, W. T.; Rouleau, C. M.; Shao-Horn, Y. The Role of Ru Redox in pH-Dependent Oxygen Evolution on Rutile Ruthenium Dioxide Surfaces. *Chem* **2017**, *2*, 668–675.

(42) Wei, C.; Sun, S.; Mandler, D.; Wang, X.; Qiao, S. Z.; Xu, Z. J. Approaches for measuring the surface areas of metal oxide electrocatalysts for determining their intrinsic electrocatalytic activity. *Chem. Soc. Rev.* **2019**, *48*, 2518–2534.

(43) Hu, J.-M.; Zhang, J.-Q.; Cao, C.-N. Oxygen evolution reaction on IrO_2-based DSA® type electrodes: kinetics analysis of Tafel lines and EIS. *Int. J. Hydrog. Energy* **2004**, *29*, 791–797.

(44) Audichon, T.; Guenot, B.; Baranton, S.; Cretin, M.; Lamy, C.; Coutanceau, C. Preparation and characterization of supported $Ru_xIr_{1-x}O_2$ nano-oxides using a modified polyol synthesis assisted by microwave activation for energy storage applications. *Appl. Catal. B* **2017**, *200*, 493–502.

(45) Soderberg, J. N.; Co, A. C.; Sirk, A. H. C.; Birss, V. I. Impact of Porous Electrode Properties on the Electrochemical Transfer Coefficient. *J. Phys. Chem. B* **2006**, *110*, 10401–10410.

(46) Co, A. C.; Birss, V. I. Mechanistic Analysis of the Oxygen Reduction Reaction at (La,Sr)MnO_3 Cathodes in Solid Oxide Fuel Cells. *J. Phys. Chem. B* **2006**, *110*, 11299–11309.

(47) Ping, Y.; Nielsen, R. J.; Goddard, W. A. The Reaction Mechanism with Free Energy Barriers at Constant Potentials for the Oxygen Evolution Reaction at the IrO_2 (110) Surface. *J. Am. Chem. Soc.* **2017**, *139*, 149–155.

(48) Schalenbach, M.; Kasian, O.; Ledendecker, M.; Speck, F. D.; Mingers, A. M.; Mayrhofer, K. J. J.; Cherevko, S. The Electrochemical Dissolution of Noble Metals in Alkaline Media. *Electrocatalysis* **2018**, *9*, 153–161.

(49) Liu, Y.; Zhou, D.; Deng, T.; He, G.; Chen, A.; Sun, X.; Yang, Y.; Miao, P. Research Progress of Oxygen Evolution Reaction Catalysts for Electrochemical Water Splitting. *ChemSusChem* **2021**, *14*, 5359–5383.

(50) Chen, L.-W.; He, F.; Shao, R.-Y.; Yan, Q.-Q.; Yin, P.; Zeng, W.-J.; Zuo, M.; He, L.; Liang, H.-W. Intermetallic IrGa-IrO_x core-shell electrocatalysts for Oxygen Evolution. *Nano Research* **2021**, *15*, 1853–1860.

(51) Zhang, J.; Wang, T.; Pohl, D.; Rellinghaus, B.; Dong, R.; Liu, S.; Zhuang, X.; Feng, X. Interface Engineering of MoS_2 /Ni_3S_2 Heterostructures for Highly Enhanced Electrochemical Overall-Water-Splitting Activity. *Angew. Chem. Int. Ed.* **2016**, *128*, 6814–6819.

(52) Gong, L.; Ren, D.; Deng, Y.; Yeo, B. S. Efficient and Stable Evolution of Oxygen Using Pulse-Electrodeposited Ir/Ni Oxide Catalyst in Fe-Spiked KOH Electrolyte. *ACS Appl. Mater. Interfaces* **2016**, *8*, 15985–15990.

(53) Guan, J.; Li, D.; Si, R.; Miao, S.; Zhang, F.; Li, C. Synthesis and Demonstration of Subnano-

metric Iridium Oxide as Highly Efficient and Robust Water Oxidation Catalyst. *ACS Catal.* **2017**, *7*, 5983–5986.

(54) Huang, T.; Moon, S. K.; Lee, J.-M. A heterostructure of layered double hydroxide wrapped in few-layer carbon with iridium doping for efficient oxygen evolution. *Electrochim. Acta* **2019**, *296*, 590–597.

(55) Zhuang, Z. et al. Three-dimensional open nano-netcage electrocatalysts for efficient pH-universal overall water splitting. *Nat. Commun.* **2019**, *10*, 4875.

(56) Wang, J.; Ji, Y.; Yin, R.; Li, Y.; Shao, Q.; Huang, X. Transition metal-doped ultrathin RuO2 networked nanowires for efficient overall water splitting across a broad pH range. *J. Mater. Chem. A* **2019**, *7*, 6411–6416.

(57) Yuan, C.-Z.; Jiang, Y.-F.; Zhao, Z.-W.; Zhao, S.-J.; Zhou, X.; Cheang, T.-Y.; Xu, A.-W. Molecule-Assisted Synthesis of Highly Dispersed Ultrasmall RuO_2 Nanoparticles on Nitrogen-Doped Carbon Matrix as Ultraefficient Bifunctional Electrocatalysts for Overall Water Splitting. *ACS Sustainable Chem. Eng.* **2018**, *6*, 11529–11535.

(58) Zhang, C.; Zhang, X.; Daly, K.; Berlinguette, C. P.; Trudel, S. Water Oxidation Catalysis: Tuning the Electrocatalytic Properties of Amorphous Lanthanum Cobaltite through Calcium Doping. *ACS Catal.* **2017**, *7*, 6385–6391.

(59) Zhang, C.; Berlinguette, C. P.; Trudel, S. Water oxidation catalysis: an amorphous quaternary Ba-Sr-Co-Fe oxide as a promising electrocatalyst for the oxygen-evolution reaction. *Chem. Commun.* **2016**, *52*, 1513–1516.

(60) Geiger, S.; Kasian, O.; Shrestha, B. R.; Mingers, A. M.; Mayrhofer, K. J. J.; Cherevko, S. Activity and Stability of Electrochemically and Thermally Treated Iridium for the Oxygen Evolution Reaction. *Journal of The Electrochemical Society* **2016**, *163*, F3132–F3138.

(61) Anantharaj, S.; Reddy, P. N.; Kundu, S. Core-Oxidized Amorphous Cobalt Phosphide Nanostructures: An Advanced and Highly Efficient Oxygen Evolution Catalyst. *Inorg. Chem.* **2017**, *56*, 1742–1756.

(62) Mathi, S.; Jayabharathi, J. Enhanced stability and ultrahigh activity of amorphous ripple nanostructured Ni-doped Fe oxyhydroxide electrode toward synergetic electrocatalytic water splitting. *RSC Adv.* **2020**, *10*, 26364–26373.

(63) Guo, C.; Sun, X.; Kuang, X.; Gao, L.; Zhao, M.; Qu, L.; Zhang, Y.; Wu, D.; Ren, X.; Wei, Q. Amorphous Co-doped MoO_x nanospheres with a core–shell structure toward an effective oxygen evolution reaction. *J. Mater. Chem. A* **2019**, *7*, 1005–1012.

(64) Cherevko, S.; Reier, T.; Zeradjanin, A. R.; Pawolek, Z.; Strasser, P.; Mayrhofer, K. J. Stability of nanostructured iridium oxide electrocatalysts during oxygen evolution reaction in acidic environment. *Electrochem. commun.* **2014**, *48*, 81–85.

(65) Jovanovič, P.; Hodnik, N.; Ruiz-Zepeda, F.; Arčon, I.; Jozinović, B.; Zorko, M.; Bele, M.; Šala, M.; Šelih, V. S.; Hočevar, S.; Gaberšček, M. Electrochemical Dissolution of Iridium and Iridium Oxide Particles in Acidic Media: Transmission Electron Microscopy, Electrochemical Flow Cell Coupled to Inductively Coupled Plasma Mass Spectrometry, and X-ray Absorption Spectroscopy Study. *J. Am. Chem. Soc.* **2017**, *139*, 12837–12846.

(66) Pedersen, A. F.; Escudero-Escribano, M.; Sebok, B.; Bodin, A.; Paoli, E.; Frydendal, R.; Friebel, D.; Stephens, I. E.; Rossmeisl, J.; Chorkendorff, I., et al. Operando XAS Study of the Surface Oxidation State on a Monolayer IrO_x on RuO_x and Ru Oxide Based Nanoparticles for Oxygen Evolution in Acidic Media. *J. Phys. Chem. B* **2018**, *122*, 878–887.

(67) Risch, M.; Morales, D. M.; Villalobos, J.; Antipin, D. What X-Ray Absorption Spectroscopy Can Tell Us About the Active State of Earth-Abundant Electrocatalysts for the Oxygen Evolution Reaction. *Angew. Chem. Int. Ed.* **2022**, *n/a*.

(68) Patterson, A. L. The Scherrer Formula for X-Ray Particle Size Determination. *Phys. Rev.* **1939**, *56*, 978–982.

(69) Langford, J. I.; Wilson, A. J. C. Scherrer after sixty years: A survey and some new results in the determination of crystallite size. *J. Appl. Crystallogr.* **1978**, *11*, 102–113.

(70) Hellenbrandt, M. The Inorganic Crystal Structure Database (ICSD) – Present and Future. *Crystallogr. Rev.* **2004**, *10*, 17–22.

(71) Gražulis, S.; Chateigner, D.; Downs, R. T.; Yokochi, A. F. T.; Quirós, M.; Lutterotti, L.; Manakova, E.; Butkus, J.; Moeck, P.; Le Bail, A. Crystallography Open Database – an open-access collection of crystal structures. *J. Appl. Crystallogr* **2009**, *42*, 726–729.

(72) Brett, C. M. A.; Brett, A. M. O. *Electrochemistry: principles, methods, and applications*; Oxford University Press: Oxford, 1993.

(73) Bard, A. J.; Faulkner, L. R. *Electrochemical methods: fundamentals and applications*; John Wiley and Sons, Inc: New York, 2001.

(74) Smith, R. D. L.; Prévot, M. S.; Fagan, R. D.; Trudel, S.; Berlinguette, C. P. Water Oxidation Catalysis: Electrocatalytic Response to Metal Stoichiometry in Amorphous Metal Oxide Films Containing Iron, Cobalt, and Nickel. *J. Am. Chem. Soc.* **2013**, *135*, 11580–11586.

(75) Walton, J.; Wincott, P.; Fairley, N.; Carrick, A. *Peak fitting with CasaXPS: a casa pocket book*; Accolyte Science, 2010.

(76) Dau, H.; Liebisch, P.; Haumann, M. X-ray absorption spectroscopy to analyze nuclear geometry and electronic structure of biological metal centers—potential and questions examined with special focus on the tetra-nuclear manganese complex of oxygenic photosynthesis. *Anal. Bioanal. Chem.* **2003**, *376*, 562–583.

(77) Ravel, B.; Newville, M. *ATHENA*, *ARTEMIS*, *HEPHAESTUS*: data analysis for X-ray absorption spectroscopy using *IFEFFIT*. *J. Synchrotron Radiat.* **2005**, *12*, 537–541.

(78) Kraft, S.; Stümpel, J.; Becker, P.; Kuetgens, U. High resolution X-ray absorption spectroscopy with absolute energy calibration for the determination of absorption edge energies. *Rev. Sci. Instrum.* **1996**, *67*, 681–687.

(79) Mustre de Leon, J.; Rehr, J. J.; Zabinsky, S. I.; Albers, R. C. *Ab-initio* curved-wave X-ray-absorption fine structure. *Phys. Rev. B* **1991**, *44*, 4146–4156.

(80) Rehr, J. J.; Albers, R. C. Scattering-matrix formulation of curved-wave multiple-scattering theory: Application to X-ray-absorption fine structure. *Phys. Rev. B* **1990**, *41*, 8139–8149.

(81) Mishra, S.; Daniele, S.; Hubert-Pfalzgraf, L. G. Metal 2-ethylhexanoates and related compounds as useful precursors in materials science. *Chem. Soc. Rev.* **2007**, *36*, 1770–1787.

(82) Nakamoto, K. *Infrared and Raman Spectra of Inorganic and Coordination Compounds*; John Wiley and Sons, Inc: New York, 1997.

(83) McCrory, C. C. L.; Jung, S.; Ferrer, I. M.; Chatman, S. M.; Peters, J. C.; Jaramillo, T. F. Benchmarking Hydrogen Evolving Reaction and Oxygen Evolving Reaction Electrocatalysts for Solar Water Splitting Devices. *J. Am. Chem. Soc.* **2015**, *137*, 4347–4357.